arXiv:2410.00147v1 [cs.CE] 30 Sep 2024

Modeling Turbulence in the Atmospheric Boundary Layer with Spectral Element and Finite Volume Methods

Ananias Tomboulides,[c] Matthew Churchfield,[b] Paul Fischer,[d,e]
Michael Sprague,[b] and Misun Min,[a]

[a] *Mathematics and Computer Science, Argonne National Laboratory, Lemont, IL, USA*

[b] *Computational Science Center, National Renewable Energy Laboratory, Golden, CO, USA*

[c] *Mechanical Engineering, Aristotle University of Thessaloniki, Tessaloniki, Greece*

[d] *Computer Science, University of Illinois Urbana-Champaign, Urbana, IL, USA*

[e] *Mechanical Science & Engineering, University of Illinois Urbana-Champaign, Urbana, IL, USA*

Corresponding author: Email address: mmin@mcs.anl.gov (Misun Min)

ABSTRACT: We present large-eddy-simulation (LES) modeling approaches for the simulation of atmospheric boundary layer turbulence that are of direct relevance to wind energy production. In this paper, we study a GABLS benchmark problem using high-order spectral element code Nek5000/RS and a block-structured second-order finite-volume code AMR-Wind which are supported under the DOE's Exascale Computing Project (ECP) Center for Efficient Exascale Discretizations (CEED) and ExaWind projects, respectively, targeting application simulations on various acceleration-device based exascale computing platforms. As for Nek5000/RS we demonstrate our newly developed subgrid-scale (SGS) models based on mean-field eddy viscosity (MFEV), high-pass filter (HPF), and Smagorinsky (SMG) with traction boundary conditions. For the traction boundary conditions, a novel analytical approach is presented that solves for the surface friction velocity and surface kinematic temperature flux. For AMR-Wind, standard SMG is used and discussed in detail the traction boundary conditions for convergence. We provide low-order statistics, convergence and turbulent structure analysis. Verification and convergence studies were performed for both codes at various resolutions and it was found that Nek5000/RS demonstrates convergence with resolution for all ABL bulk parameters, including boundary layer and low level jet (LLJ) height. Extensive comparisons are presented with simulation data from the literature.

1. Introduction

Accurate simulations of the atmospheric boundary layer (ABL) are central to engineering design questions related to wind farms, buildings, and urban canyons. In this paper, we explore turbulence modeling for the ABL in the context of two general-purpose codes that are capable of supporting the complex geometries required of engineering design codes, namely the spectral element code, Nek5000/RS, Fischer et al. (2008, 2021)[1] and the finite-volume code, AMR-Wind, Sprague et al. (2020); Sharma et al. (2024). These codes were developed as part of the U.S. Department of Energy's Exascale Computing Project and are designed to run on both CPU- and GPU-based platforms. Extensive performance studies for the GEWEX (Global Energy and Water Cycle Experiment) Atmospheric Boundary Layer Study (GABLS) Beare et al. (2006) are presented in Min et al. (2023a). Here, we explore the impacts of discretizations, subgrid-scale LES models, and wall models on mean and rms velocity and temperatures profiles on turbulence morphology, and on the energy spectra. We present inter-code comparisons and comparisons with results in the literature, including the pseudospectral results of Sullivan et al. (2008).

ABL flows feature turbulent mixing, vertical diffusion, vertical and horizontal heat exchanges, and Coriolis effects due to planetary rotation and curvature, with the additional complexity from the regional-scale weather patterns and terrain. Significant studies have been applied to ABL flows Moeng (1984); Sullivan et al. (2008); Churchfield and Moriarty (2020). We focus on high-order numerical computation of stably stratified ABL flows using large eddy simulation (LES). The governing equations, incompressible Navier–Stokes (NS), are solved in filtered form such that the larger, energy-containing eddies are directly resolved, and the remaining SGS turbulence is modeled. The stably stratified atmospheric boundary layer is a key component of Earth-system modeling, as well as of large-scale weather, climate, and ocean models Fernando and Weil (2010), Mahrt (2014), Large et al. (1994), McWilliams (2004), Cuxart et al. (2006), Svensson and Holtslag (2009), Holtslag et al. (2013), Heisel et al. (2023).

The ABL community has set up a sequence of benchmark problems, the GEWEX (Global Energy and Water Cycle Experiment) Atmospheric Boundary Layer Study (GABLS) Beare et al. (2006), to quantify the effects of numerical modeling and discretization choices. These benchmarks represent the atmospheric boundary layer in regional and large-scale. Atmospheric models are considered

[1]Nek5000/RS represents the two codes, Nek5000 and NekRS where NekRS is a GPU variant of Nek5000.

important benchmarks for improving modeling approaches for the study of wind energy, climate, and weather on all scales Rodrigo et al. (2017).

In this paper, we consider the GABLS1 benchmark, illustrated in Fig. 1, which is a well-documented stably-stratified flow problem. The studies are conducted using the Argonne-developed open-source Navier–Stokes (NS) solver, Nek5000/RS, which is based on high-order spectral element (SE) discretizations Deville et al. (2002). NekRS Fischer et al. (2021) is a GPU-accelerated version of Nek5000 Fischer et al. (2008) developed under the ECP CEED project, targeting application simulations on various acceleration-device based exascale computing platforms Fischer et al. (2021); Min et al. (2022).

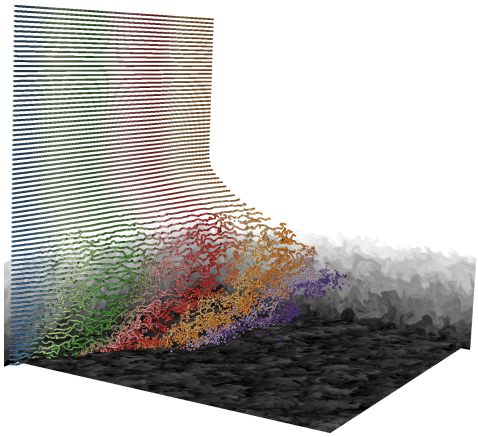

Fig. 1: NekRS simulation for the atmospheric boundary layer flows with particle tracer (Simulation by Lidquist Lindquist et al. (2021).

In our earlier reports Min and Tomboulides (2022), Min et al. (2023b), we demonstrated our newly developed SGS models based on the work of Sullivan et al. (1994), Moeng and Sullivan (2015) that involve the use of a mean-field eddy viscosity (MFEV) in conjunction with either a high-pass filter (HPF) method, an algebraic Smagorinsky method, or the solution of an SGS turbulent kinetic energy equation (TKE) for the isotropic small scale motion. The model fidelity and scaling performance of Nek5000/RS on DOE's leadership computing platforms in comparison with that of AMR-Wind, a block-structured second-order finite-volume code with adaptive-mesh-refinement capabilities, were discussed in Min et al. (2024). Here we focus on model fidelity of Nek5000/RS in comparison to that of AMR-Wind as well as issues related to numerical convergence.

This paper is organized as follows. Section 2 presents the governing equations for our LES modeling approach. Section 3 briefly describes the GABLS benchmark problem, Section 4 discusses our SGS models, and Section 4 presents verification and convergence studies. Section 5 presents the way the traction boundary conditions are obtained, and Section 6 contains the results obtained with the newly implemented SGS models. In Section 7 we present some of the conclusions from our study.

2. Large Eddy Simulation Model

For the atmospheric LES, we consider the governing equations consisting of the incompressible Navier–Stokes (NS) and potential temperature equations in nondimensional form, solved in a *spatially filtered* resolved-scale formulation defined as

$$\frac{\partial \bar{u}_i}{\partial t} + \bar{u}_j \frac{\partial \bar{u}_i}{\partial x_j} = -\frac{1}{\bar{\rho}} \frac{\partial \bar{p}}{\partial x_i} - \frac{\partial \tau_{ij}}{\partial x_j} + f_i - \frac{\theta'}{\theta_0} g_i, \tag{1}$$

$$\frac{\partial \bar{u}_j}{\partial x_j} = 0, \tag{2}$$

$$\frac{\partial \bar{\theta}}{\partial t} + \bar{u}_j \frac{\partial \bar{\theta}}{\partial x_j} = -\frac{\partial \tau_{\theta j}}{\partial x_j}, \tag{3}$$

where $\bar{u}_i$ is the ith component of the resolved-scale velocity vector, $\bar{\rho}$ is the density, $\bar{p}$ is the pressure, g_i is the gravity acceleration vector, and $\bar{\theta}$ is the potential temperature in the resolved scale. The scalar θ'/θ_0 in the buoyancy force is defined by

$$\frac{\theta'}{\theta_0} = \frac{\bar{\theta} - \theta_0}{\theta_0}, \tag{4}$$

where θ_0 is the reference potential temperature. f_i represents the Coriolis acceleration defined by

$$f_i = -2\epsilon_{i3k}\Omega\bar{u}_k, \tag{5}$$

where ϵ_{ijk} is the alternating unit tensor and Ω is the planetary rotation rate vector at the point of interest on the planet (which is dependent on latitude), and $j = 3$ corresponds to the vertical direction.

In addition, τ_{ij} and $\tau_{\theta j}$ are the stress tensors in the momentum and energy equations including SGS modeling terms defined as

$$\tau_{ij} = -\frac{2}{Re} S_{ij} + \tau_{ij}^{sgs} = -\frac{1}{Re}\left(\frac{\partial \bar{u}_i}{\partial x_j} + \frac{\partial \bar{u}_j}{\partial x_i}\right) + \tau_{ij}^{sgs}, \tag{6}$$

and

$$\tau_{\theta j} = -\frac{1}{Pe}\frac{\partial \bar{\theta}}{\partial x_j} + \tau_{\theta j}^{sgs}, \tag{7}$$

where Re is the Reynolds number, Pe is the Peclet number, S_{ij} is the resolved-scale strain-rate tensor, and τ_{ij}^{sgs} and $\tau_{\theta j}^{sgs}$ are the SGS stress tensors.

3. ABL GABLS Benchmark

We consider the GABLS benchmark problem Beare and et. al (2006) which is a stable ABL where the ground temperature is cooler than the air temperature and continues to cool over the duration of the simulation. We define the domain as $\Omega = L_x \times L_y \times L_z = 400$ m $\times$ 400 m $\times$ 400 m, with the streamwise direction x, the spanwise direction y, and the vertical direction z. We initialize our simulations at time $t = 0$ with a constant velocity in the streamwise direction equal to the geostrophic wind speed of $U = 8$ m/s. We define the initial potential temperature by 265 K in $0 \leq z \leq 100$ m and linearly increase at a rate of 0.01 K/m in the range of 100 m $\leq z \leq 400$ m. The reference potential temperature is 263.5 K. The Reynolds number is $Re = UL_b/\nu$, where $L_b = 100$ m is the thickness of the initial thermal boundary layer and ν is the molecular viscosity, and it is $\approx 50M$, which precludes direct numerical simulation (DNS) wherein all turbulent scales are resolved. We add an initial perturbation to the temperature with an amplitude of 0.1 K on the potential temperature field for $0 \leq z \leq 50$ m.

Periodic boundary conditions (BCs) are used in the streamwise and spanwise directions. At the top boundary, ($z = 400$ m), a stress-free, rigid lid is applied for momentum, and the heat flux for the energy equation is set consistent with the 0.01 K/m temperature gradient initially prescribed in the upper region of the flow. At the bottom boundary, we perform simulations with impenetrable traction BCs for the velocity, where the specified shear stress comes from Monin-Obukhov similarity theory Monin and Obukhov (1954). For the energy equation, a heat flux is applied that is derived from the same theory and a specified potential temperature difference between the flow at a height, z_1, and the surface. The surface temperature is from the GABLS specification following the rule $\theta_b(t) = 265 - 0.25t$, where t is in hours. Because the boundary conditions are periodic (lateral), or the mass flow rate through the boundaries is zero (top and bottom), pressure boundary conditions are not needed.

4. SGS Modeling Approaches in Nek5000/NekRS

We have extended the range of SGS modeling approaches in Nek5000/NekRS based on the MFEV approach of Sullivan et al. (1994) and have implemented three different ways to include

small0scale isotropic motion as described in our earlier ANL reports, Min and Tomboulides (2022) and Min et al. (2023b). Our SGS modeling approaches investigated are summarized below,

Model Name	SGS Anisotropic	SGS Isotropic
MFEV/HPF	MFEV	HPF
MFEV/SMG	MFEV	SMG
MFEV/SGS-TKE	MFEV	SGS-TKE

where HPF refers to the high pass filter of Stolz et al. (2005), SMG to the algebraic Smagorinsky model Smagorinsky (1963), and TKE to the solution of a SGS turbulent kinetic energy equation Sullivan et al. (1994).

We consider traction boundary conditions (BCs) along the lower wall in all simulations discussed here, in which the normal velocity component is set to zero and traction BCs are specified for the two horizontal velocity components; in addition, heat flux BCs are specified for the potential temperature, based on the Monin-0Obukhov log law Monin and Obukhov (1954).

We implemented the traction BCs for the horizontal velocity components in the context of the log law, following the approach of Grotjans and Menter (1998) and Kuzmin et al. (2007), which is suitable for finite element methods based on a weighted residual formulation. The traction BCs imposed on the tangential velocity are based on the horizontally averaged slip velocity that develops at the boundary or at a specified sampling $z-$location from the lower wall.

The SGS stress tensors τ_{ij}^{sgs} and $\tau_{\theta j}^{sgs}$ are expressed in terms of a non-isotropic part, $\left\langle \tau_{ij}^{sgs} \right\rangle$, and an isotropic part, τ'_{ij}. Thus, the sub-grid-scale dissipation is based on a non-isotropic MFEV ν_T, obtained by the horizontally averaged mean strain rate, and an isotropic, fluctuating part ν_t. The law of the wall is effected through the use of the MFEV concept, and the approach originally by Schumann (1975) is used to convert the horizontally averaged traction to local values based on the local slip velocity in each of the horizontal directions. The SGS model of Sullivan et al. (1994) for the momentum is based on the following expression:

$$\tau_{ij}^{sgs} = \left\langle \tau_{ij}^{sgs} \right\rangle + \tau'_{ij} = -2\nu_T \left\langle S_{ij} \right\rangle - 2\gamma\nu_t S_{ij}. \tag{8}$$

For the energy equation, the definition of $\tau_{\theta j}$ is

$$\tau_{\theta j} = \left\langle \tau_{\theta z}^{sgs} \right\rangle + \tau'_{\theta j} = -\nu_\Theta \frac{\partial \langle \theta \rangle}{\partial z} - \nu_\theta \frac{\partial \theta}{\partial x_j}, \tag{9}$$

where $\langle\ \rangle$ denotes averaging over the homogeneous directions and ν_T is an average eddy viscosity, which is expressed in terms of mean flow quantities. In Eq. (8), γ is an "isotropy factor," which accounts for variability in the SGS constants due to anisotropy of the mean flow. When the fluctuating (isotropic) part of turbulent motion is taken into account through the use of the fluctuating strain rate, ν_t in Eq. (8) is nonzero and the full stress tensor has to be taken into account. The diffusivities ν_Θ and ν_θ in (9) are given by $\nu_\Theta = \nu_T/Pr_t$ and $\nu_\theta = \gamma\nu_t/Pr_t$, where Pr_t is either 1 or 1/3(Sullivan et al. (1994)). Thus, the momentum and potential temperature equations are given by

$$\frac{\partial \bar{u}_i}{\partial t} + \bar{u}_j \frac{\partial \bar{u}_i}{\partial x_j} = -\frac{\partial \bar{p}}{\partial x_i} - \frac{\partial \tau_{ij}}{\partial x_j} - 2\epsilon_{i3k}\Omega\bar{u}_k + (1-\delta_{i3})\frac{\partial}{\partial z}\nu_T\frac{\partial\langle\bar{u}_i\rangle}{\partial z} - \frac{\theta'}{\theta_0}g_i \tag{10}$$

$$= -\frac{\partial \bar{p}}{\partial x_i} + \frac{\partial}{\partial x_j}\left(\frac{1}{\mathrm{Re}} + \gamma\nu_t\right)2S^n_{ij} - 2\epsilon_{i3k}\Omega\bar{u}_k + (1-\delta_{i3})\frac{\partial}{\partial z}\nu_T\frac{\partial\langle\bar{u}_i\rangle}{\partial z} - \frac{\theta'}{\theta_0}g_i, \tag{11}$$

$$\frac{\partial \bar{\theta}}{\partial t} + \bar{u}_j \frac{\partial \bar{\theta}}{\partial x_j} = \frac{\partial}{\partial x_j}\left(\frac{1}{\mathrm{Pe}} + \frac{\gamma\nu_t}{Pr_t}\right)\frac{\partial\bar{\theta}}{\partial x_j} + \frac{\partial}{\partial z}\frac{\nu_T}{Pr_t}\frac{\partial\langle\bar{\theta}\rangle}{\partial z}. \tag{12}$$

The expression for the MFEV ν_T is derived so that the law-of-the-wall behavior can be recovered in the absence of any resolved turbulence, as explained below. Following Sullivan et al. (1994), we impose a "constant flux", traction-type boundary condition at $z = z_1$, which states that the sum of the SGS and resolved momentum fluxes be equal to the surface stress, i.e.,

$$\left[\left\langle\tau^{sgs}_{uw}\right\rangle^2 + \left\langle\tau^{sgs}_{vw}\right\rangle^2\right]^{1/2} + \left[\langle uw\rangle^2 + \langle vw\rangle^2\right]^{1/2} = u_\tau^2. \tag{13}$$

As described in Min and Tomboulides (2022), this traction boundary condition in Nek is imposed at the first grid point in the vertical direction, which is assumed to be a point inside the log layer at a location $z = z_1$, where the boundary condition for the vertical velocity component is defined to be zero. For this reason the second term in Eq. (13) corresponding to the resolved momentum fluxes is identically equal to zero. In Sullivan et al. (1994), a predictive relationship for the MFEV at the first grid point z_1, $\nu_T^\star = \nu_T(z_1)$ is obtained by invoking the approximation that the fluctuating components of strain are neglected compared with the mean strain so that only the horizontally

averaged SGS stress in Eq. (8) is retained. This leads to

$$\left\langle \tau_{uw}^{sgs} \right\rangle = -\nu_T \frac{\partial \langle u \rangle}{\partial z}, \\ \left\langle \tau_{vw}^{sgs} \right\rangle = -\nu_T \frac{\partial \langle v \rangle}{\partial z}. \tag{14}$$

A model for MFEV at any height, which is consistent with this idea is as follows:

$$\nu_T = \nu_T^{\star} \frac{\kappa z_1}{u_\tau \phi_m(z_1)} \sqrt{2 \left\langle S_{ij} \right\rangle \left\langle S_{ij} \right\rangle}, \tag{15}$$

where u_τ is the friction velocity, κ the von Karman constant, and ϕ_m the Monin-Obukhov stability function for momentum. The expression for $\nu_T^{\star}$ is

$$\nu_T^{\star} = \frac{u_\tau \kappa z_1}{\phi_m(z_1)}. \tag{16}$$

Equation (16) provides an adaptive method for estimating the MFEV needed to force the computed wind speed derivative to match with similarity theory at $z = z_1$. In contrast to Sullivan et al. (1994), a similar correction was also applied to the SGS potential temperature field, and $\tau_{\theta z}^{sgs}$ becomes

$$\left\langle \tau_{\theta z}^{sgs} \right\rangle = -\frac{\nu_T}{Pr_t} \frac{\partial \langle \theta \rangle}{\partial z}. \tag{17}$$

In our approach, following Grotjans and Menter (1998) and Kuzmin et al. (2007), as was described in the previous subsection, in our approach the boundary of the computational domain is not located exactly at the wall but at a finite distance from the wall corresponding to a fixed value of $z_1^+ = z/z_0$. Strictly speaking, this implies that a boundary layer of width z_1 (corresponding to the specified value of z_1^+) should be removed from the computational domain; however, it is assumed that this width is very small at high Reynolds numbers and can be considered negligible, so that the equations can be solved in the whole domain with traction BCs prescribed on the lower boundary. Since the choice of z_1^+ is rather arbitrary, we have found that values of z_1^+ up to 10 at the target Re produce averaged results that do not differ significantly.

In all apporaches described below for the modeling of the small-scale isotropic motion, the SGS dissipation is effected through a non-isotropic MFEV obtained by the horizontally-averaged mean

strain rate. In the HPF approch, the isotropic, fluctuating, part of the SGS modeling is taken into account through the use of a high-pass filter of Stolz et al. (2005), which is not eddy-viscosity based and thus for this case ν_t in (8) is equal to zero. Instead, an additional term of the form $-\chi H_N * \bar{u}_i$ and $-\chi H_N * \bar{\theta}$ is added to the momentum and energy equations, respectively, as explained in Min and Tomboulides (2022).

In the SMG approach, the isotropic, fluctuating part is taken into account through an algebraic Smagorinsky (SMG) model based on the fluctuating strain rate. The expression used for the isotropic part of the eddy viscosity ν_t is

$$\nu_t = (C_s \Delta)^2 \sqrt{2 S'_{ij} S'_{ij}}, \tag{18}$$

and S'_{ij} is given by

$$S'_{ij} = S_{ij} - \langle S_{ij} \rangle .$$

The Smagorinsky constant C_s is written in terms of C_k and C_ε as

$$C_s = \left(C_k \sqrt{\frac{C_k}{C_\epsilon}} \right)^{1/2} . \tag{19}$$

From Sullivan et al. (1994), the SGS constants are $C_k = 0.1$ and $C_\varepsilon = 0.93$. The isotropy factor γ is obtained from

$$\gamma = \frac{S'}{S' + \langle S \rangle}, \tag{20}$$

where

$$\langle S \rangle = \sqrt{2 \langle S_{ij} \rangle \langle S_{ij} \rangle}. \tag{21}$$

and

$$S' = \sqrt{2 \left\langle S'_{ij} S'_{ij} \right\rangle}, \tag{22}$$

In the third approach, TKE, a transport equation is solved for the SGS turbulent kinetic energy equation,according to Sullivan et al. (1994):

$$\left(\frac{\partial}{\partial t} + u_j \frac{\partial}{\partial x_j} \right) e = 2\gamma \nu_t S'_{ij} S'_{ij} + \frac{g}{\theta_0} \tau_{\theta z} - C_\varepsilon \frac{e^{3/2}}{L} + \frac{\partial}{\partial x_i} \left(\frac{1}{\mathrm{Re}} + 2\gamma \nu_t \right) \frac{\partial e}{\partial x_i}, \tag{23}$$

where the fluctuating eddy viscosity, ν_t, is given by

$$\nu_t = C_k L e^{1/2}. \tag{24}$$

The model length scale L that appears in the SGS TKE equation (23) and in expression (24) for the fluctuating eddy viscosity is obtained as follows. For unstable stratification, the length scale L is defined by

$$L = L_{SMG} = \Delta,$$

while for stable stratification, L is reduced as suggested by Deardorff (1980) and is obtained by the following expression:

$$L = L_{DRD} = \frac{0.76 e^{1/2}}{\left(\frac{g}{\theta_0}\frac{\partial\theta}{\partial z}\right)^{1/2}}.$$

The definition of $\tau_{\theta z}$ is

$$\tau_{\theta z} = -\nu_\theta \frac{\partial \theta'}{\partial z},$$

where

$$\theta' = \theta - \langle\theta\rangle$$

The constant C_ε is given from

$$C_\varepsilon = 0.19 + 0.74 L/\Delta.$$

We have the SGS constant $C_k = 0.1$; $C_\varepsilon = 0.93$ for the case $L = L_{SMG} = \Delta$, whereas it is variable for the case $L = L_{DRD}$. All other quantities such as S'_{ij}, γ, and $\langle S\rangle$ are defined as in the second case SMG.

5. Traction Boundary Condition

Following Schumann (1975), the exact form of the traction boundary condition corresponding to the local value of the momentum flux for each of the two horizontal components of the tangential velocity $\mathbf{u}_t = \mathbf{u} - \mathbf{n}(\mathbf{n}\cdot\mathbf{u})$, and for the case where the normal to the boundary direction is aligned with the z-direction, is obtained as follows:

$$\mathbf{t}_w = \tau_w \frac{\mathbf{u}_t}{|\mathbf{u}_t|}, \tag{25}$$

where

$$\tau_w = u_\tau^2. \tag{26}$$

The momentum flux at the boundary is based on a horizontally averaged value of the friction velocity u_τ obtained by using the law of the wall for rough walls which for the velocity and temperature is defined as

$$u^+ = \frac{|\mathbf{u}_t|}{u_\tau} = \frac{1}{\kappa}\left(\ln\frac{z_1}{z_0} + \beta_m \frac{z_1}{L}\right), \tag{27}$$

$$\theta^+ = \frac{|\Delta\theta|}{\theta_\tau} = \frac{1}{\kappa}\left(\ln\frac{z_1}{z_0} + \beta_h \frac{z_1}{L}\right), \tag{28}$$

where κ is the von Karman constant, z_1 the location of the lower wall and z_0 is a roughness related length scale; $\mathbf{u}_t$ is the velocity vector parallel to the wall, and $\Delta\theta$ is the difference between the actual wall temperature located at $z = 0$ and the temperature at z_1^+ which is the location of the lower boundary in the computation. The constants β_m and β_h are in general not equal to each other and their values are usually taken to be 4.8 and 7.2, respectively. The boundary conditions are implemented through the derivatives of the above quantities in the wall normal z direction as follows:

$$\frac{\partial|\mathbf{u}_t|}{\partial z} = \frac{u_\tau}{\kappa z_1}\phi_m \quad \text{and} \quad \frac{\partial|\theta|}{\partial z} = \frac{\theta_\tau}{\kappa z_1}\phi_h, \tag{29}$$

where

$$\phi_m\left(1 + \beta_m \frac{z_1}{L}\right) \quad \text{and} \quad \phi_h\left(1 + \beta_h \frac{z_1}{L}\right). \tag{30}$$

The value of u_τ is coupled with the corresponding value of θ_τ through the Monin-Obukhov lentgh L defined as

$$L = u_\tau^2\left(\frac{\kappa g \theta_\tau}{\theta_0}\right)^{-1}. \tag{31}$$

The values of u_τ and θ_τ are obtained by solving the two-equation system (28); and its solution procedure is described below. Rewriting equations (28) and using definition (31), we obtain the following system:

$$\begin{aligned} \left(\ln\frac{z_1}{z_0}\right)u_\tau^2 - \kappa U u_\tau + \beta_m \kappa g z \tilde{\theta}_\tau = 0, \\ \beta_h \kappa g z \tilde{\theta}_\tau^2 + \left(\ln\frac{z_1}{z_0}\right)u_\tau^2 \tilde{\theta}_\tau - \kappa \Delta\tilde{\theta} u_\tau^2 = 0, \end{aligned} \tag{32}$$

where $U = |\langle \mathbf{u}_t \rangle|$ is the absolute value of the horizontally averaged slip velocity in the horizontal direction and $\Delta\tilde{\theta} = |\langle \Delta\theta \rangle|/\theta_0$ is the nondimensional absolute value of the horizontally averaged temperature difference between the wall temperature located at $z = 0$ and the computed temperature at z_1 which is the location of the lower boundary of the computational domain. Both $\langle \mathbf{u}_t \rangle$ and $\langle \Delta\theta \rangle$ are obtained from the velocity and temperature solutions at the previous timestep during the simulation. In system (32) the only unknowns are u_τ and $\tilde{\theta}_\tau = \theta_\tau/\theta_0$ and the solution can be obtained analytically as

$$\tilde{\theta}_{\tau 1,2} = \frac{u_{\tau 1,2}}{\beta_m \kappa g z_1}\left(\kappa U - u_{\tau 1,2}\ln\frac{z_1}{z_0}\right), \tag{33}$$

and

$$u_{\tau 1,2} = \frac{1}{2}\frac{2\frac{\beta_h}{\beta_m} - 1}{\frac{\beta_h}{\beta m} - 1}\frac{\kappa U}{\ln\frac{z_1}{z_0}}\left[1 \pm \frac{\sqrt{\Delta}}{\left(2\frac{\beta_h}{\beta_m} - 1\right)}\right], \tag{34}$$

where Ri is the bulk Richardson number with $Ri = g z_1 \Delta\tilde{\theta}/U^2$ and $\Delta = 1 + 4Ri\,(\beta_h - \beta_m)$. For the case that β_m and β_h are assumed to be equal, the solution simplifies to

$$\begin{aligned} u_\tau &= \frac{\kappa U}{\ln\frac{z_1}{z_0}}\left(1 - \beta_m Ri\right), \\ \tilde{\theta}_\tau &= \frac{\kappa \Delta\tilde{\theta}}{\ln\frac{z_1}{z_0}}\left(1 - \beta_m Ri\right), \end{aligned} \tag{35}$$

which is the same solution as that obtained by Basu et al. (2008). However, when the constants β_m and β_h are not equal and assuming that $\beta_h > \beta_m$, the general solution is given by (33) and (34). We note that only one of the two solutions for u_τ in (34) leads to a positive value for θ_τ, and this is the smallest root $u_{\tau 2}$, which corresponds to the negative sign in front of Δ. Thus, this is

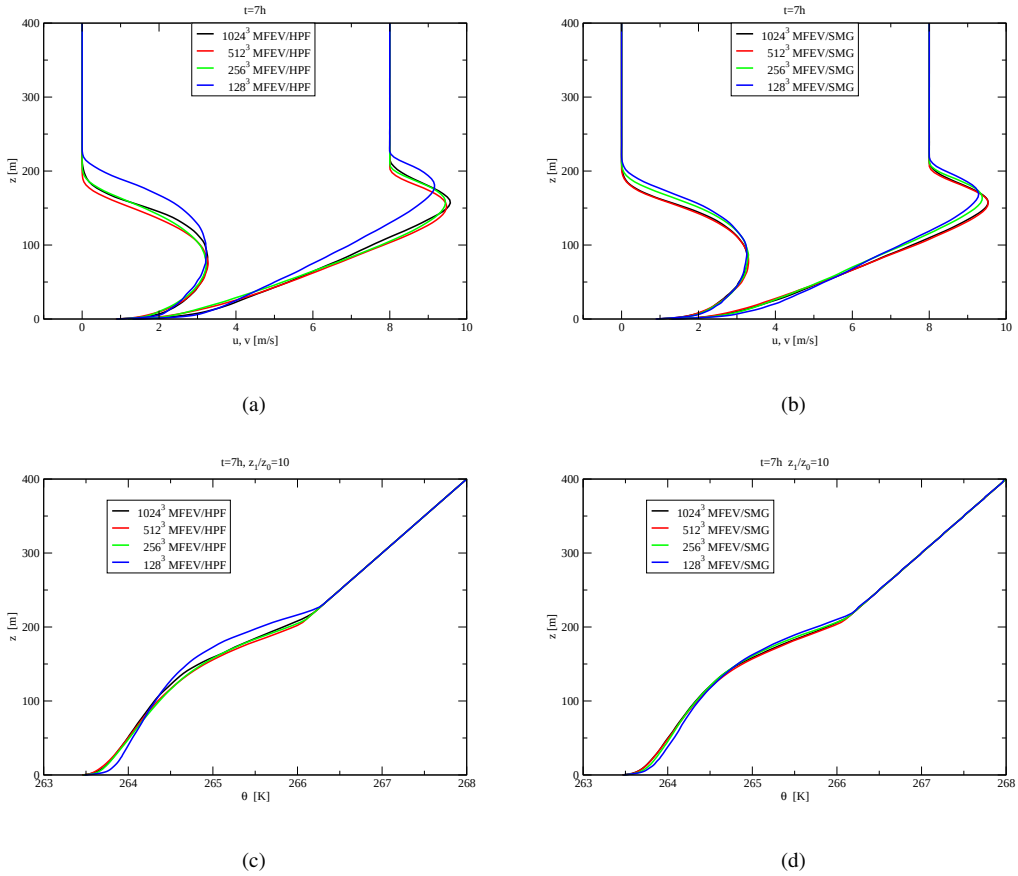

FIG. 2: Nek5000/RS Convergence in horizontally averaged velocity with (a) MEFV/HPF and (b) MFEV/SMG and potential temperature profiles at $t = 7h$ with (c) MEFV/HPF and (d) MFEV/SMG.

the solution used to specify u_τ and θ_τ in our computations when traction BCs are used for the horizontal velocities.

6. Convergence and Verification Tests

Results obtained with both the MFEV/HPF approach and the MFEV/SMG approach lead to converged results with increasing resolution as well as to asymptotic convergence with Re and z_1^+. Moreover, convergence with resolution seems to be faster with resolution using MFEV/SMG as compared with MFEV/HPF as can be observed in Fig. 2 (a) and (b), which show horizontally averaged streamwise and spanwise velocities at $t = 7h$ using MFEV/SMG and MFEV/HPF, respec-

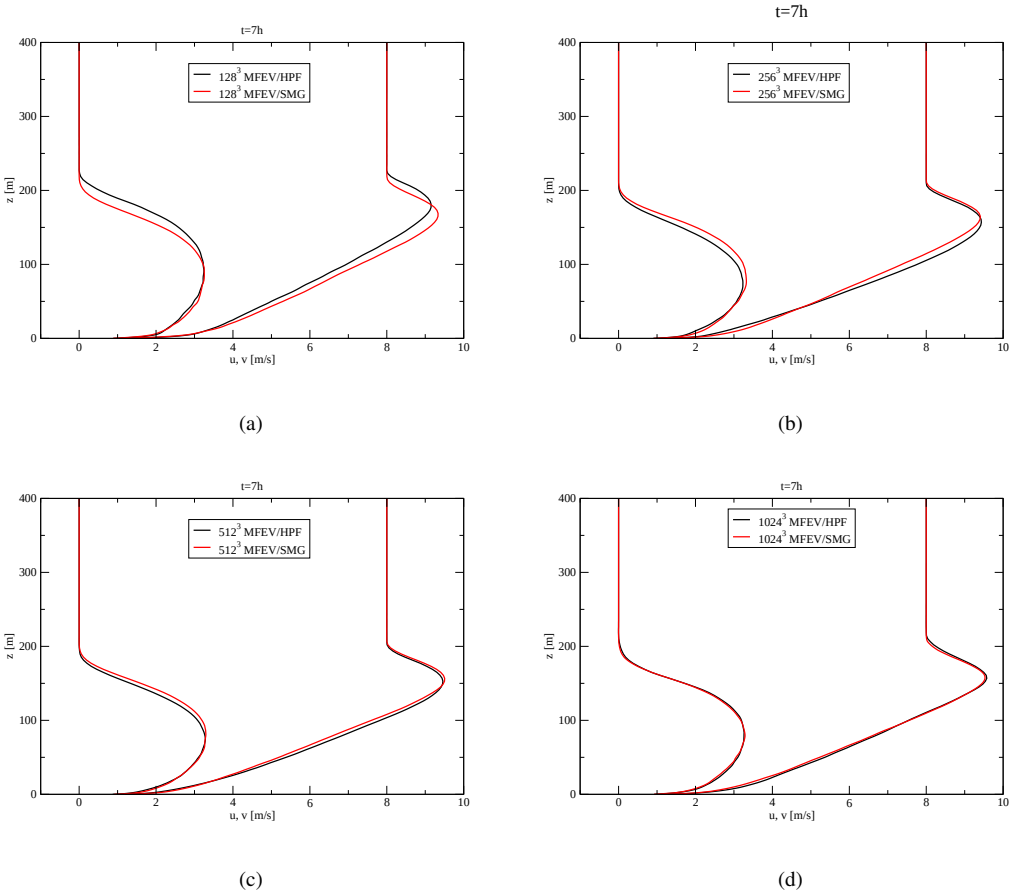

FIG. 3: Nek5000/RS Comparison between mean profiles obtained with MEFV/HPF and MFEV/SMG with resolution (a) $n = 128^3$, (b) $n = 256^3$, (c) $n = 512^3$, and (d) $n = 1024^3$.

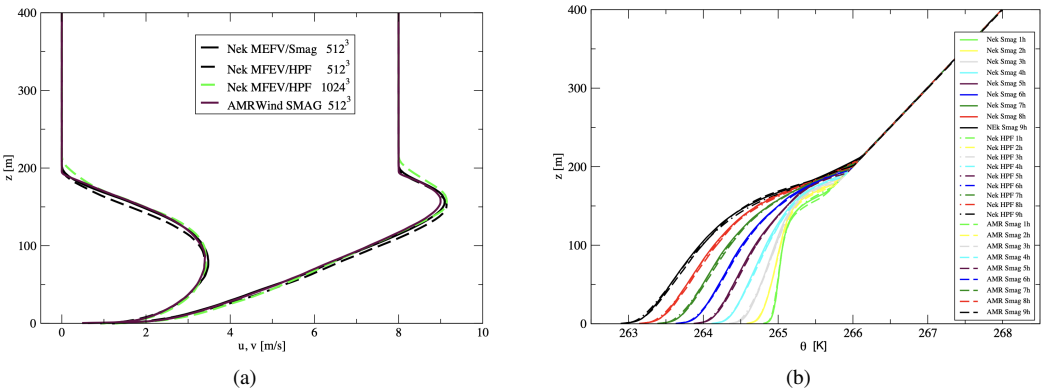

FIG. 4: Nek5000/RS horizontally averaged (a) streamwise, spanwise velocities and (b) potential temperature at $t = 6h$ using MFEV/SMG and MFEV/HPF with traction boundary conditions, compard with AMR-Wind for 512^3.

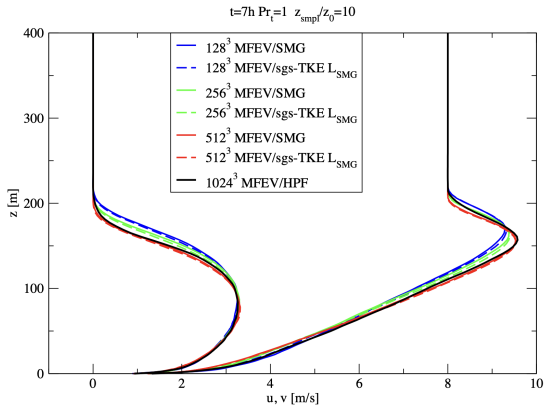

FIG. 5: Nek5000/RS Convergence for MEFV/SMG and MFEV/HPF.

tively, using traction boundary conditions. The same behavior can be observed in Fig. 2 (c) and (d) which shows horizontally averaged profiles of potential temperature for the same two appoaches.

Interestingly, the difference between the mean profiles obtained with MFEV/HPF and MFEV/SMG is reduced with increasing resolution as can be observed in Fig. 3 (a)–(d).

Figure 4 (a) shows the horizontally averaged streamwise and spanwise velocities and Fig. 4(b) the horizontally averaged potential temperature at $t = 6h$ for the two highest resolutions 512^3 and 1024^3 for Nek5000/RS MFEV/HPF and MFEV/SMG and for 512^3 for AMR-Wind, respectively. As can be observed, Nek5000/RS converges to the same profiles as resolution is increased; they also agree well with the AMR-Wind obtained profiles at 512^3.

Figure 5 compares horizontally averaged streamwise and spanwise velocity profiles at $t = 7h$, using MFEV/SMG and MFEV/SGS-TKE with L_{SMG} for resolutions $n = 128^3$, $n = 256^3$ and $n = 512^3$. For completeness, the MFEV/HPF profiles for $n = 1024^3$ are also shown. As can be observed, the difference between MFEV/SMG and MFEV/SGS-TKE using L_{SMG} is negligible for all resolutions.

In addition to the above, sampling for the evaluation of the wall momentum and heat fluxes was extended to include specified $z-$locations away from the lower wall. Specifically, as explained in Min et al. (2023b), it was possible to sample tangential velocities and potential temperature at specified $z-$locations away from the lower wall in order to evaluate u_τ and θ_τ, i.e. the wall momentum and heat fluxes. The evaluation of u_τ and θ_τ is performed using the system of equations and method presented in section 4 of Min and Tomboulides (2022). To investigate the effect of

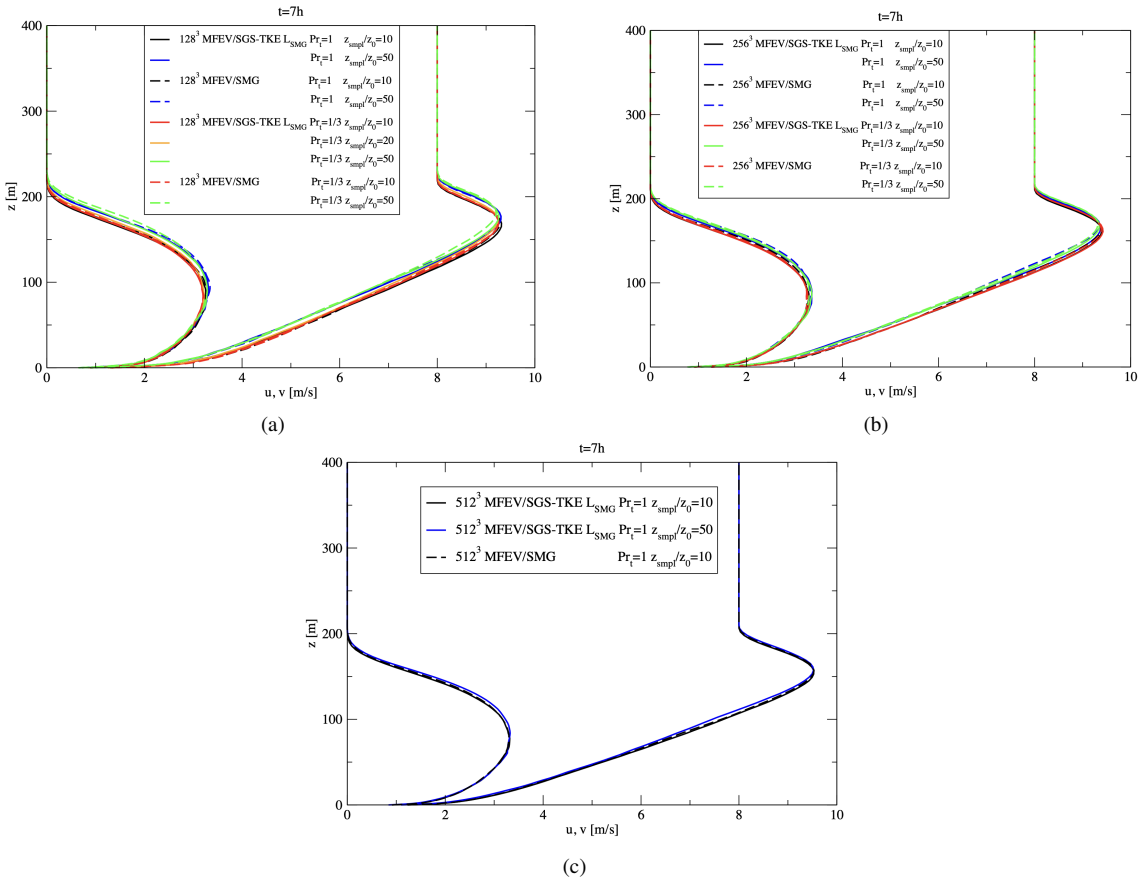

FIG. 6: Nek5000/RS, The effect of sampling location: horizontally averaged streamwise and spanwise velocity profiles at $t = 7h$ using z_{smpl}/z_0 values between 10 and 50 for resolutions (a) $n = 128^3$, (b) $n = 256^3$, and (c) $n = 512^3$.

the sampling location z_{smpl} on the results, simulations using MFEV/SGS-TKE with L_{SMG} were performed for various values of z_{smpl}/z_0 ranging between 10 and 50, for various resolutions. Figure 6 shows horizontally averaged streamwise and spanwise velocity profiles at $t = 7h$ using z_{smpl}/z_0 values between 10 and 50 for resolutions (a) $n = 128^3$, (b) $n = 256^3$, and (c) $n = 512^3$. An important conclusion from this study was that the effect of the sampling location diminishes with resolution and already at $n = 512^3$ it is almost negligible.

The effect of Pr_t was also investigated for the case MFEV/SGS-TKE with L_{SMG} and the results are shown in Fig. 7 (a) and (b) at resolutions $n = 128^3$, and $n = 256^3$, with Pr_t taking values 1 and $1/3$ for $z_{smpl}/z_0 = 10$ and $z_{smpl}/z_0 = 50$, respectively. As can be observed, the effect of Pr_t is almost negligible for both resolutions studied.

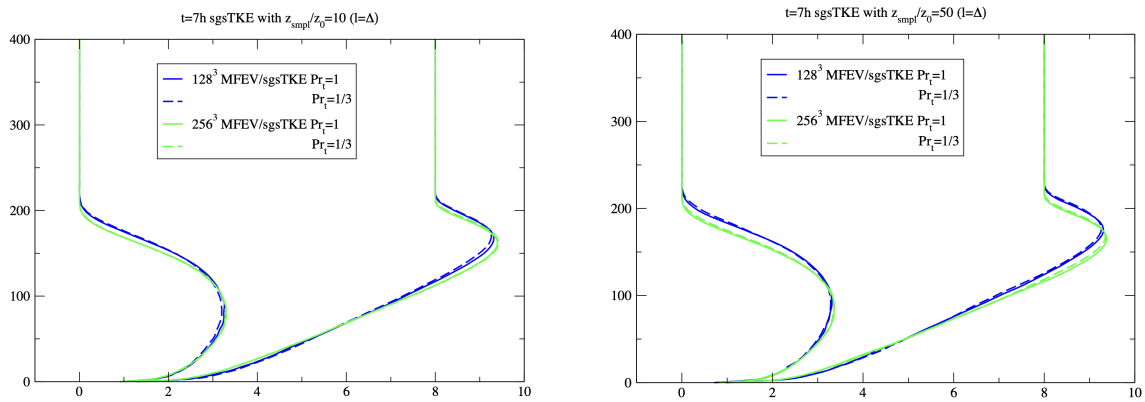

(a) (b)

FIG. 7: Nek5000/RS, The effect of Pr_t: horizontally averaged streamwise and spanwise velocity profiles at $t = 7h$ at resolutions 128^3, and 256^3, using (a) $z_{smpl}/z_0 = 10$ and (b) $z_{smpl}/z_0 = 50$, with Pr_t taking values 1 and $1/3$.

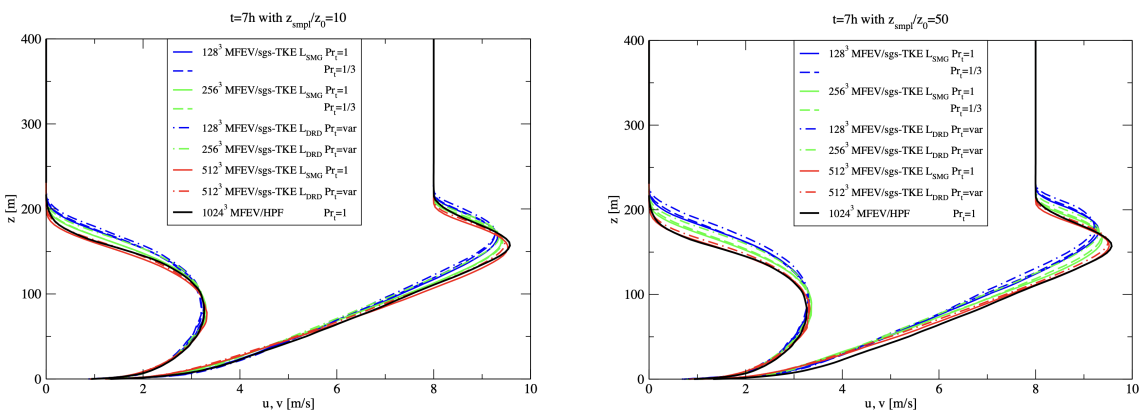

(a) (b)

FIG. 8: Nek5000/RS, Horizontally averaged streamwise and spanwise velocity profiles at $t = 7h$ for resolutions $n = 128^3$, $n = 256^3$, and $n = 512^3$ using MFEV/SGS-TKE and L_{SMG} vs L_{DRD} for (a) $z_{smpl}/z_0 = 10$ and (b) $z_{smpl}/z_0 = 50$.

Figure 8 shows a comparison of the horizontally averaged streamwise and spanwise velocity profiles at $t = 7h$ for (a) $z_{smpl}/z_0 = 10$ and (b) $z_{smpl}/z_0 = 50$, between the MFEV/SGS-TKE with L_{SMG} and the MFEV/SGS-TKE with L_{DRD} for resolutions $n = 128^3$, $n = 256^3$, and $n = 512^3$. For completeness, the MFEV/HPF profiles for $n = 1024^3$ are also shown. As resolution is increased, differences between profiles obtained by the two approaches, MFEV/SGS-TKE with L_{SMG} and MFEV/SGS-TKE with L_{DRD}, become negligible.

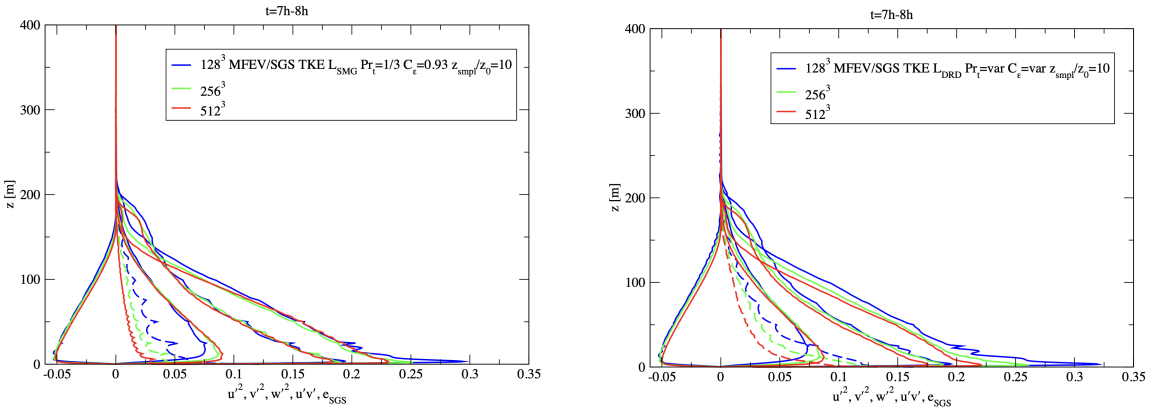

(a) (b)

FIG. 9: Nek5000/RS, Horizontally averaged streamwise, spanwise and normal fluctuation profiles at $t = 7h$ for $z_{smpl}/z_0 = 10$ using (a) MFEV/SGS-TKE with L_{SMG} and (b) MFEV/SGS-TKE with L_{DRD} for resolutions $n = 128^3$, $n = 256^3$, and $n = 512^3$.

Figure 9 shows a comparison of the horizontally averaged streamwise, spanwise and normal fluctuation profiles at $t = 7h$ for $z_{smpl}/z_0 = 10$ using (a) MFEV/SGS-TKE with L_{SMG} and (b) MFEV/SGS-TKE with L_{DRD} for resolutions $n = 128^3$, $n = 256^3$, and $n = 512^3$. Good convergence is also observed in second-order quantities in Fig. 9 (a) and (b), for MFEV/SGS-TKE with (a) L_{SMG} and with (b) L_{DRD}. This is especially the case for resolutions $n = 256^3$ and $n = 512^3$ and for L_{SMG}. The resolved fluctuations obtained by the two approaches MFEV/SGS-TKE+with L_{SMG} and L_{DRD} compare reasonably well for the same effective resolution.

7. GABLS results from Nek5000/NekRS and AMR-Wind

Table 1 provides a summary of the simulation details and bulk boundary layer values from simulations of the GABLS case using five grids with increasing resolution, N = (128^3, 256^3, 512^3, 1024^3, 2048^3). The variables in Table 1 are the case, the effective resolution, the approximate total number of timesteps, the mesh spacing, the average surface friction velocity u_τ, the average surface kinematic temperature flux $Q^\star$, boundary-layer depth z_i, Monin-Obukhov stability length $L_{MO} = -u_\tau^3/\kappa\beta Q^\star$ with von Karman constant $\kappa = 0.4$, and boundary-layer stability parameter z_i/L_{MO}. The height of the low-level jet (LLJ) or wind maximum defined as the vertical location z_j, where the horizontal velocity reaches a maximum is also included in the last column. In contrast to Sullivan et al. (2016) the ABL depth z_i is defined as the height where the vertical gradient of the

Table 1: Global quantities

Run	Pts	N_{steps}	Δ(m)	z_i (m)	$u_\tau \left(\text{m s}^{-1}\right)$	$Q^\star \times 10^3 \left(\text{Kms}^{-1}\right)$	L_{MO} (m)	z_i/L_{MO}	z_j/z_i
A	128^3	140000	3.125	223.8	0.266	-10.24	122.978	1.82	0.74
B	256^3	266000	1.56	217.9	0.264	-9.89	124.385	1.752	0.74
C	512^3	540000	0.78	212.9	0.257	-9.41	121.745	1.749	0.72
D	1024^3	1400000	0.39	215.7	0.257	-9.44	120.747	1.786	0.71
E	2048^3	3200000	0.19	216.4	0.259	-9.68	120.747	1.796	0.72

horizontal velocity drops to negligible values and is not based on the maximum vertical gradient of the mean potential temperature. The ABL height z_i as well as $u_\tau, Q^\star, L_{MO}$, z_i/L_{MO}, and z_j/z_i appear to be converging with grid resolution. In contrast, in Sullivan et al. (2016) and McWilliams et al. (2023) these parameters were found to vary with the grid resolution primarily because of the variability in z_i. Statistics, denoted by angle brackets are obtained by averaging in the x-y planes and over the time period $8 < t < 9h$. A turbulent fluctuation from a horizontal mean is denoted by a superscript prime $()'$.

In addition to the bulk quantities in Table 1, our analysis of the stable ABL includes computation of vertical profiles of low-order moments, namely, means, variances, and momentum and temperature fluxes. Figures 10, left and right, compare horizontally and time-averaged profiles of streamwise/spanwise velocity and potential temperature, respectively for $8 < t < 9h$, using MFEV/TKE for resolutions $N = 128^3$, $N = 256^3$, $N = 512^3$, $N = 1024^3$, and $N = 2048^3$. In these figures the vertical coordinate was not normalized with the boundary-layer depth, and as can be observed, the profiles above a resolution of $N = 512^3$ do not appreciably change; the same holds for the boundary-layer depth. The same profiles from the work of Sullivan et al. (2016) at resolution of 1024^3 are shown in the same figures for comparison.

For AMR-Wind, the planar and time averaged profiles of streamwise and spanwise velocities are shown in Fig. 11, left, and of potential temperature Fig. 11, right. Again the same profiles from the work of Sullivan et al. (2016) at resolution of 1024^3 are shown in the same figures for comparison.

The horizontally and time averaged profiles of the magnitude of the horizontal velocity and wind direction for Nek5000/RS are shown in Fig. 12, left and right, respectively. The same figures from the work of Sullivan et al. (2016) at resolution of 1024^3 are shown in the same figures for comparison.

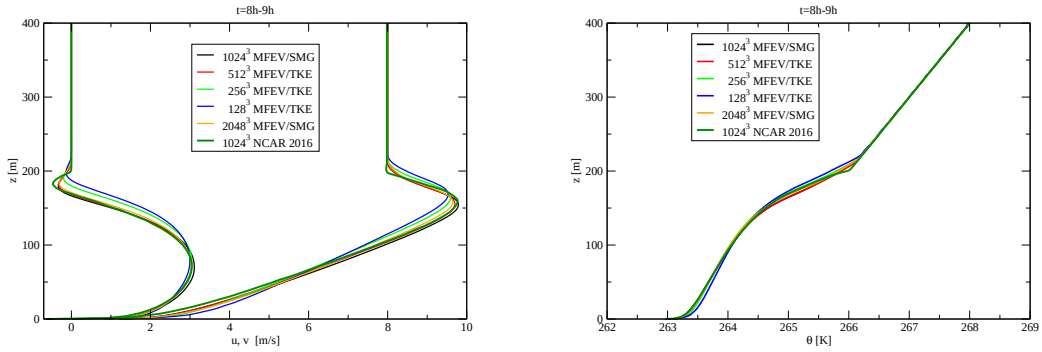

(a) (b)

FIG. 10: Planar and time averaged profiles of streamwise/spanwise velocity (left) and potential temperature (right) for $8 < t < 9h$, using MFEV/TKE for resolutions $N = 128^3$, $N = 256^3$, $N = 512^3$, $N = 1024^3$ and $N = 2048^3$.

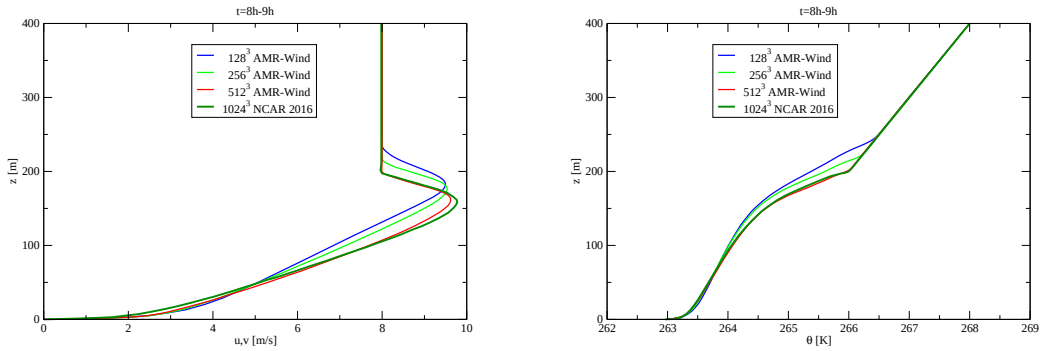

(a) (b)

FIG. 11: Vertical profiles of planar averaged u and v-velocity (left) and of planar averaged potential temperature from AMR-Wind.

The vertical profiles of the planar and time averaged horizontal velocity and wind direction for AMR-Wind are shown in Fig. 13, left and right, respectively, together with same profiles from Sullivan et al. (2016) at resolution of 1024^3.

A similar behavior is observed in Fig. 14, left, for horizontally and time averaged fluctuations between $8 < t < 9h$. This figure compares fluctuation profiles obtained using MFEV/TKE normalized with $(u^\tau)^2$ for resolutions $N = 128^3$, $N = 256^3$, $N = 512^3$ and $N = 1024^3$. SGS contributions are

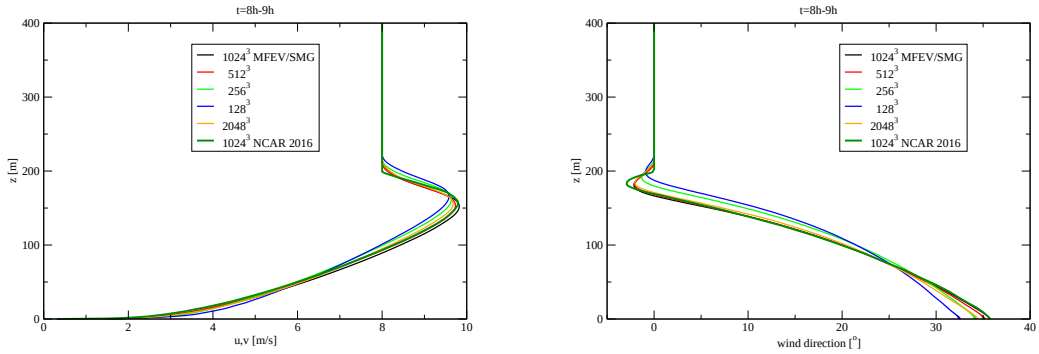

(a) (b)

FIG. 12: Nek5000/RS planar and time averaged for $8 < t < 9h$ horizontal velocity (left) and wind direction (right), using MFEV/TKE for resolutions $N = 128^3$, $N = 256^3$, $N = 512^3$ and $N = 1024^3$

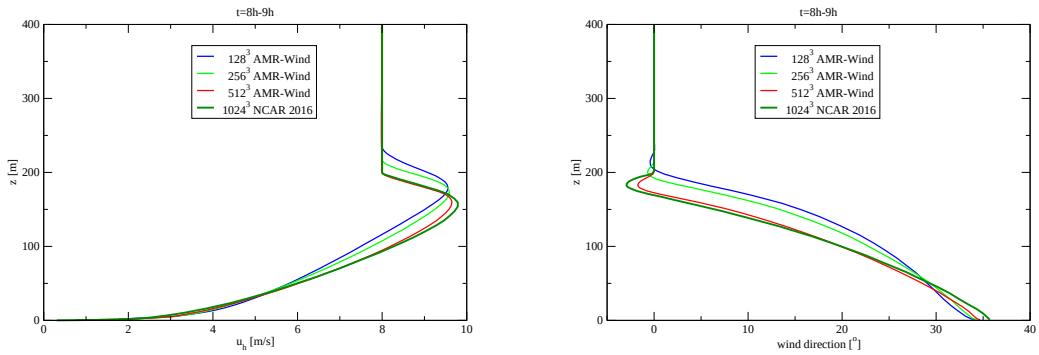

(a) (b)

FIG. 13: Vertical profiles of planar averaged averaged horizontal velocity (left) and wind direction (right) AMR-Wind for resolutions $N = 128^3$, $N = 256^3$, $N = 512^3$.

included to all quantities in the figure and as can be seen observed, the profiles do not appreciably change above $N = 256^3$. In this figure, the lower resolution simulations at $N = 128^3$, $N = 256^3$ were repeated with non-uniform resolution in the vertical direction to reduce spikes at interelemental boudaries. This is a common feature of spectral element simulations, which however, does not affect convergence of these quantities. Except for the spikes, the profiles are almost identical to the profiles obtained using uniform resolution (dashed). As can be observed, the velocity variances

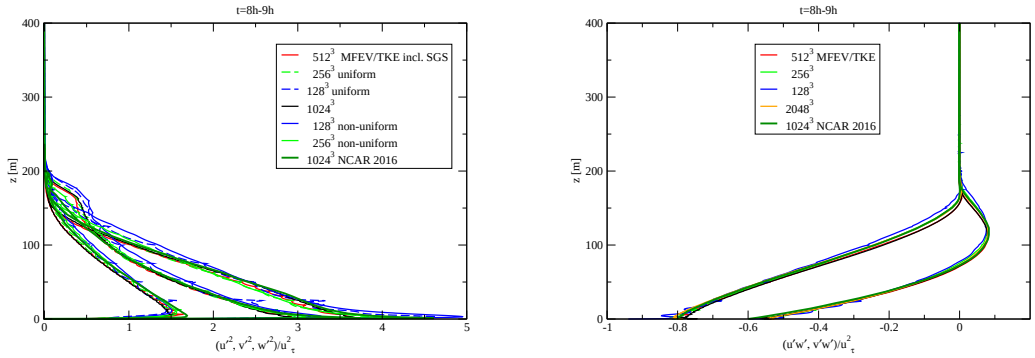

(a) (b)

FIG. 14: Nek5000/RS, MFEV/TKE fluctuation velocity profiles incl. SGS (left) and variance and covariance profiles incl. SGS (right) with resolution.

from all simulations, which include SGS contributions collapse quite well for the four higher mesh resolutions considered.

The same holds for the streamwise and. spanwise vertical momentum fluxes $\langle u'w' \rangle$ and $\langle u'v' \rangle$ that include both the resolved and SGS contributions, which are shown in Fig. 14, right, and which are in close agreement as the mesh spacing varies for all resolutions.

The streamwise and spanwise vertical momentum fluxes $\langle u'w' \rangle$ and $\langle u'v' \rangle$ that include both the resolved and SGS contributions for AMR-Wind are shown in 15 together with the same profiles from Sullivan et al. (2016).

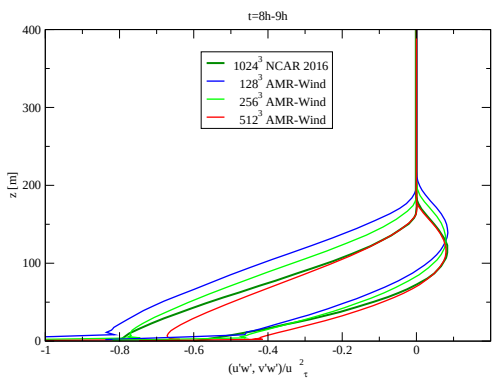

FIG. 15: Vertical profiles of velocity variance from AMR-Wind.

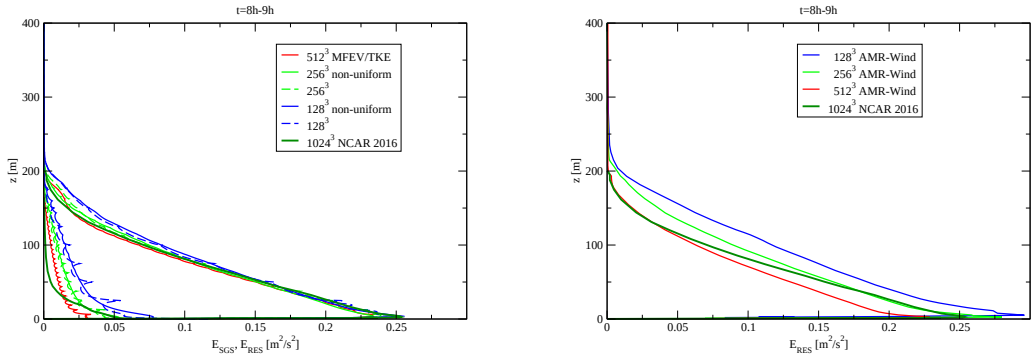

(a) (b)

FIG. 16: Vertical profiles of resolved and SGS turbulent kinetic energy from Nek5000/RS (left) and of resolved turbulent kinetic energy from AMR-Wind (right).

A measure of the resolved nature of the flow fields is provided in Fig. 16. The vertical profiles of resolved and SGS turbulent kinetic energy from Nek5000/RS are shown in Fig. 16, left, and profiles of resolved turbulent kinetic energy from AMR-Wind are shown in 16, right. As can be observed, the SGS energy computed near the surface is less than 20% of the total for the coarsest resolution $N = 128^3$, and reduces to values below 10% at a resolution of 512^3. This ratio is reduced to even smaller values at the highest resolution of 1024^3. The profile of SGS energy shown in Fig. 16 shows a systematic decrease with resolution over the whole stable ABL. In fact, as noted in McWilliams et al. (2023) the SGS TKE scales with $\Delta^{2/3}$ which corresponds to an approximate reduction of 40% with a mesh size reduction by a factor of 2.

The vertical profiles of the squared shear and buoyancy frequency (S^2, N^2) from Nek5000/RS simulations are shown in Fig. 17 (a) for the four resolutions considered. Here

$$N^2 = \frac{g}{\theta_0}\frac{\partial\langle\theta\rangle}{\partial z}, \tag{36}$$

and

$$S^2 = \left(\frac{\partial\langle\mathbf{u}_h\rangle}{\partial z}\right), \tag{37}$$

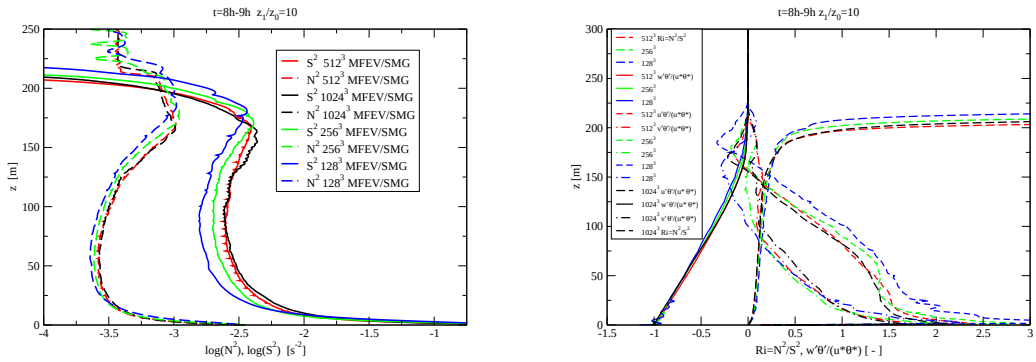

(a) (b)

FIG. 17: (a) MFEV/SMG N^2 and S^2 profiles with resolution and (b) MFEV/SMG heat flux and Ri profiles.

where $\mathbf{u}_h$ is the horizontal velocity. The Richardson number Ri, defined as

$$Ri(z) = \frac{N^2}{S^2}, \tag{38}$$

is shown together with the vertical and horizontal temperature fluxes, which include SGS contributions, in Fig. 17 (b). As can be observed, the profiles are in close agreement as the mesh spacing is reduced. In agreement with Sullivan et al. (2016), above the LLJ, $z > z_j$, S^2, and N^2 both decrease but at rates sufficient to maintain a constant Ri near or slightly below the critical value of 0.25. We note that a value of $Ri(z) \approx 0.2$ shows the approximate validity of the simple RANS parameterization of a constant Richardson number above the Monin–Obukhov surface layer. The profiles of the vertical, $\langle w'\theta' \rangle$, and horizontal temperature fluxes, $\langle w'\theta' \rangle$ and $\langle w'\theta' \rangle$ are normalized by the product of the surface values $u^\tau Q^\star$. As can be observed from the figure, in the mid- to lower BL, the vertical temperature fluxes are near-linear functions of z as expected Sullivan et al. (2016). In the upper region, the mean flux profile displays more curvature, and approaching z_i the vertical flux nearly collapses because of the increasing stratification. The horizontal temperature fluxes are comparable in magnitude to the vertical flux throughout the bulk of the BL. Futhermore, although the vertical temperature flux converges very quickly with resolution, the horizontal temperature fluxes seem to converge slower with increasing resolution.

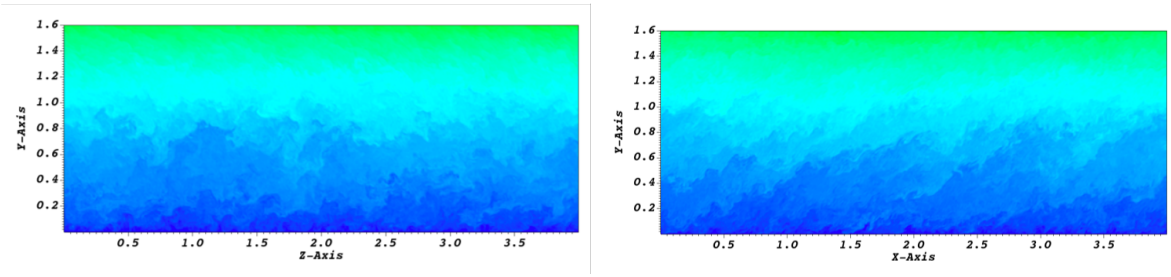

(a) (b)

FIG. 18: Nek5000/RS Instantaneous potential temperature isocontours at $t = 9h$ at (a) $y = 200$ m and (b) at $x = 300$ m.

Figures 18 (a) and (b) show the instantaneous temperature isocontours at $t = 9h$ in an x–z plane at $y = 200$ m and a $y - z$ plane at $x = 300$ m, respecively. In agreement with Sullivan et al. (2016), inspection of these figures reveals that the temperature fronts are sharp warm - cold fronts tilted in the downstream direction, primarily a consequence of the sheared streamwise velocity. Near the low-level jet (z between 150-160m), the fronts are weaker with values of tilt angle.

Figure 19 shows the instantaneous temperature isocontours in an $x - z$ plane at $z = 100$ m for the two codes Nek5000/RS and AMR-Wind and for three different resolutions. As can be observed, finer scales do get resolved by both codes as resolution increases. However, the same scales seem to be resolved by the high-order Nek5000/RS code using half the resolution of AMR-Wind. For example, the finest-resolved scales in the upper middle and lower right figures are very similar, and they correspond to 256^3 for Nek5000/RS and 512^3 for AMR-Wind.

Figure 20 demonstrates the spatial spectrum for velocity magnitude at $t = 8h$ and at $z = 100$ m for $N = 256^3$, 512^3, 1024^3, and 2048^3 resolutions. We can observe that Nek is able to resolve out to nx/π, as would be expected given that the max spacing for the collocation points is $(\pi/2)(L/nx)$, rather than (L/nx), for which Nyquist dictates that one can resolve only to $nx/2$. Beyond (nx/π), we have a viscous-like decay, which corresponds to SGS dissipation. On the other hand, the same spectrum obtained with AMR-Wind using a resolution of 512^3 is almost identical with the one obtained by Nek using a resolution of 256^3. This is attributed to the second order spatial convergence of AMR-Wind compared with the hgih-order spectral convergence of Nek.

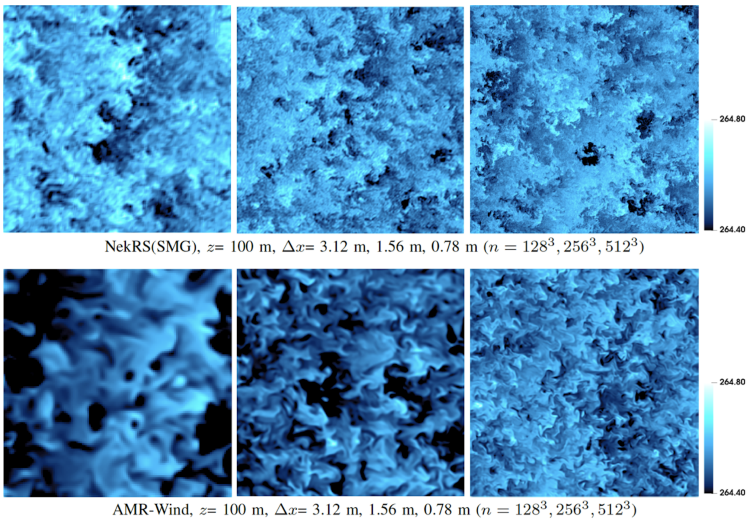

FIG. 19: Nek5000/RS MFEV/SMG and AMR-Wind at three grid refinement levels for potential temperature at $t = 6h$.

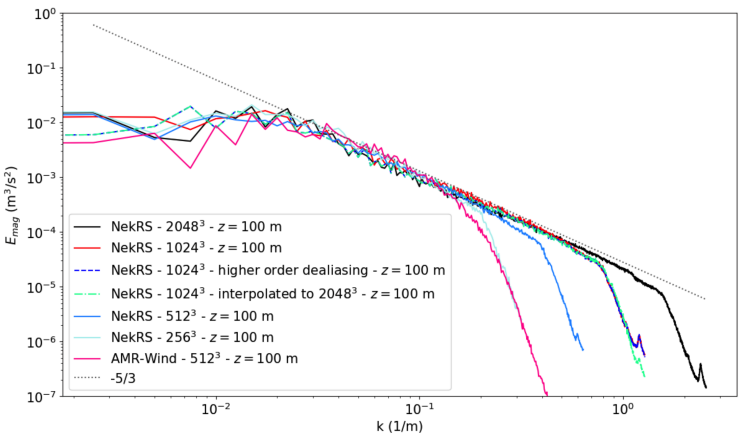

FIG. 20: Nek5000/RS and AMR-Wind: Spatial spectrum of the horizontal velocity at z = 100m with resolution.

The remaining Fig. 21 (a)–(c) show the comparison of Nek5000/RS to the NCAR, IMUK, and MO results for the surface momentum flux, the surface heat flux, and the Monin-Obukhov length, respectively.

8. Conclusion

We presented high-fidelity LES turbulence models for the atmospheric boundary layer flows. We considered the GABLS1 benchmark problem and extended the range of our SGS modeling

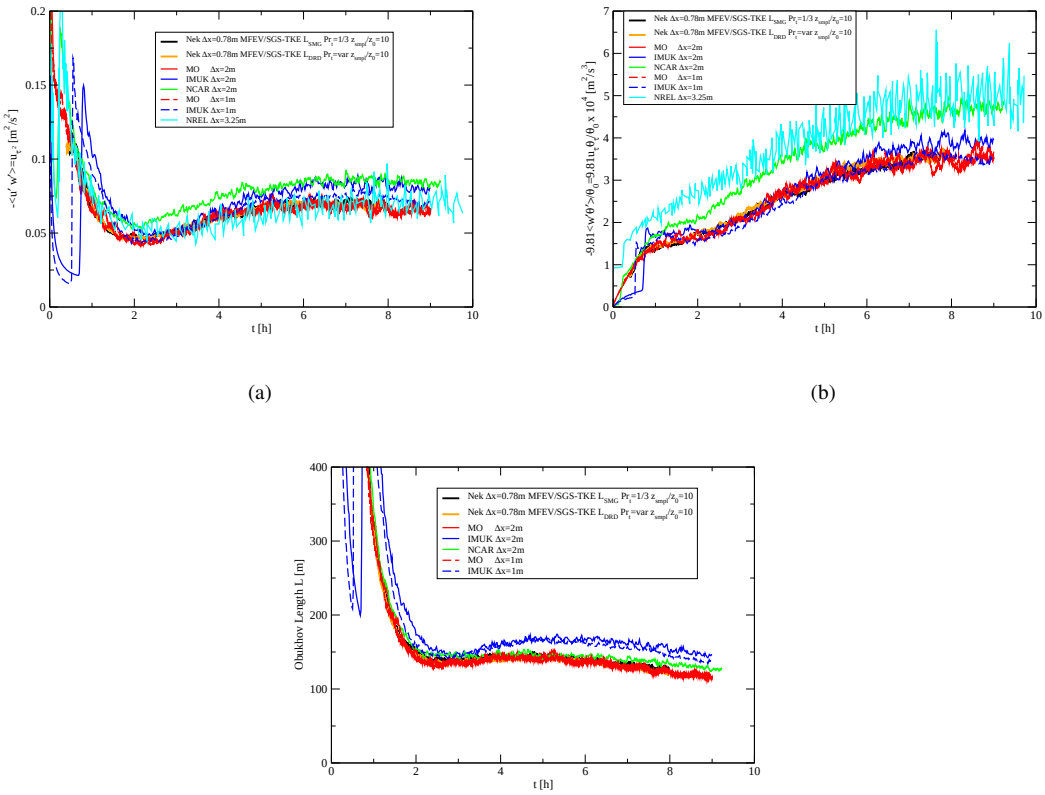

(a) (b)

(c)

FIG. 21: Comparison of Nek5000/RS with the NCAR, IMUK, and MO results for (a) the surface momentum flux, (b) the surface heat flux, and (c) the Monin-Obukhov length with resolution of 256^3, 512^3, 1024^3, and 2048^3.

approaches in the context of the mean-field eddy viscosity provided with cross-verification and validation of two different codes, Nek5000/RS and AMR-Wind, that are based on unstructured high-order and structured low-order order discretizations.

Acknowledgments

This research was supported by the U.S. Department of Energy, Office of Science, under contract DE-AC02-06CH11357 and by the Exascale Computing Project (17-SC-20-SC), a joint project of the U.S. Department of Energy Office of Science and the National Nuclear Security Administration, responsible for delivering a capable exascale ecosystem, including software, applications, and

hardware technology, to support the nation's exascale computing imperative. Funding was also provided by the U.S. Department of Energy, Office of Energy Efficiency and Renewable Energy, Wind Energy Technologies Office. This work was authored in part by the National Renewable Energy Laboratory, operated by Alliance for Sustainable Energy, LLC, for the U.S. Department of Energy (DOE) under Contract No. DE-AC36-08GO28308. The research used resources at the Oak Ridge Leadership Computing Facility at Oak Ridge National Laboratory, which is supported by the Office of Science of the U.S. Department of Energy under Contract DE-AC05-00OR22725. The research also used computational resources sponsored by the DOE Office of Energy Efficiency and Renewable Energy and located at the National Renewable Energy Laboratory. Part of this work has been supported by funding from the European High-Performance Computing Joint Undertaking and Sweden, Germany, Spain, Greece and Denmark under the CEEC project, Grant agreement No101093393. The highest resolution simulations of 2048^3 were performed at the Gauss Centre for Supercomputing, on the GCS Supercomputer JUWELS at Julich Supercomputing Centre (JSC) under project LESABL.

References

Basu, S., A. Holtslag, V. D. Wiel, A. F. Moene, and G. J. Steeneveld, 2008: An inconvenient truth about using sensible heat flux as a surface boundary condition in models under stably stratified regimes. *Acta Geophysica*, **56 (1)**, 88–99.

Beare, R., and et. al, 2006: An intercomparison of large-eddy simulations of the stable boundary layer. *Boundary-Layer Meteorology*, **(118)**, 247–272.

Beare, R. J., and Coauthors, 2006: An intercomparison of large-eddy simulations of the stable boundary layer. *Boundary-Layer Meteorology*, **118 (2)**, 247–272.

Churchfield, M., and P. Moriarty, 2020: Modeling and simulation of wind-farm flows. *Wind Energy Modeling and Simulation: Volume 1: Atmosphere and Plant*, Inst. Eng. and Tech., 217–271.

Cuxart, J., A. Holtslag, R. Beare, and et al., 2006: Single-column model intercomparison for a stably stratified atmospheric boundary layer. *Boundary-Layer Meteorol*, **118**, 273–303, https://doi.org/https://doi.org/10.1007/s10546-005-3780-1.

Deardorff, J. W., 1980: Stratocumulus-capped mixed layers derived from a three-dimensional model. *Bound.-Layer Meteor.*, **18**, 495–527.

Deville, M., P. Fischer, and E. Mund, 2002: *High-order methods for incompressible fluid flow*. Cambridge University Press, Cambridge.

Fernando, H., and J. C. Weil, 2010: Whither the stable boundary layer. *Bull. Amer. Meteor. Soc.*, **91**, 1475–1484, URL https://doi.org/10.1175/2010BAMS2770.1.

Fischer, P., J. Lottes, and S. Kerkemeier, 2008: Nek5000: Open source spectral element CFD solver. http://nek5000.mcs.anl.gov and https://github.com/nek5000/nek5000.

Fischer, P., and Coauthors, 2021: Nekrs, a gpu-accelerated spectral element navier-stokes solver. *CoRR*, **abs/2104.05829**, URL https://arxiv.org/abs/2104.05829, 2104.05829.

Grotjans, H., and F. Menter, 1998: Wall functions for general application CFD codes. *ECCOMAS 98, Proceedings of the 4th European Computational Fluid Dynamics Conference, John Wiley & Sons*, 1112–1112.

Heisel, M., P. Sullivan, G. Katul, and et al., 2023: Turbulence organization and mean profile shapes in the stably stratified boundary layer: Zones of uniform momentum and air temperature. *Boundary-Layer Meteorol*, **186**, 533–565, https://doi.org/https://doi.org/10.1007/s10546-022-00771-0.

Holtslag, A., and Coauthors, 2013: Stable atmospheric boundary layers and diurnal cycles: Challenges for weather and climate models. *Bulletin of the American Meteorological Society*, **94 (11)**, 1691–1706, https://doi.org/10.1175/BAMS-D-11-00187.1.

Kuzmin, D., O. Mierka, and S. Turek, 2007: On the implementation of the Îº-Îµ turbulence model in incompressible flow solvers based on a finite element discretisation. *International Journal of Computing Science and Mathematics*, **1 (2-4)**, 193–206, https://doi.org/10.1504/IJCSM.2007.016531.

Large, W. G., J. C. McWilliams, and S. C. Doney, 1994: Oceanic vertical mixing: A review and a model with a nonlocal boundary layer parameterization. *Reviews of Geophysics*, **32 (4)**, 363–403, https://doi.org/https://doi.org/10.1029/94RG01872.

Lindquist, N., M. Min, and P. Fischer, 2021: Scalable interpolation on gpus for thermal fluids applications. Tech. Rep. ANL-21/55, Argonne National Laboratory.

Mahrt, L., 2014: Stably stratified atmospheric boundary layers. *Annual Review of Fluid Mechanics*, **46**, 23–45, https://doi.org/https://doi.org/10.1146/annurev-fluid-010313-141354.

McWilliams, J., C. Meneveau, E. Patton, and P. Sullivan, 2023: Turbulent winds and temperature fronts in large-eddy simulations of the stable atmospheric boundary layer. *Atmosphere*, **14 (1107)**, URL https://doi.org/10.3390/atmos14071107.

McWilliams, J. C., 2004: Phenomenological hunts in two-dimensional and stably stratified turbulence. *Atmospheric Turbulence and Mesoscale Meteorology: Scientific Research Inspired by Doug Lilly*, E. Fedorovich, R. Rotunno, and B. Stevens, Eds., Cambridge University Press, 35–50.

Min, M., M. Brazell, A. Tomboulides, M. Churchfield, P. Fischer, and M. Sprague, 2023a: Towards exascale for wind enery simulations, revision.

Min, M., M. Brazell, A. Tomboulides, M. Churchfield, P. Fischer, and M. Sprague, 2024: Towards exascale for wind enery simulations. *The International Journal of High Performance Computing Applications*, **38(4)**, 337–355, https://doi.org/10.1177/10943420241252511.

Min, M., and A. Tomboulides, 2022: Simulating atmospheric boundary layer turbulence with Nek5000/RS. Tech. Rep. ANL-22/79, Argonne National Laboratory.

Min, M., A. Tomboulides, P. Fischer, M. Churchfield, and M. Sprague, 2023b: Advanced turbulence models for large-scale atmospheric boundary layer flows. Tech. Rep. ANL-23/60, Argonne National Laboratory.

Min, M., and Coauthors, 2022: Optimization of full-core reactor simulations on summit. *2022 International Conference for High Performance Computing, Networking, Storage, and Analysis*, 1–11.

Moeng, C., and P. Sullivan, 2015: *Large-eddy simulation*, Vol. 4. Academic Press, 232–240 pp.

Moeng, C.-H., 1984: A large-eddy-simulation model for the study of planetary boundary-layer turbulence. *Journal of the Atmospheric Sciences*, **41 (13)**, 2052–2062.

Monin, A. S., and A. M. Obukhov, 1954: Basic laws of turbulent mixing in the surface layer of the atmosphere. *Tr. Akad. Nauk. SSSR Geophiz. Inst.*, **24 (151)**, 163–187.

Rodrigo, J., M. Churchfield, and B. Kosovic, 2017: A methodology for the design and testing of atmospheric boundary layer models for wind energy applications. *Wind Energ. Sci.*, **2**, 23–54.

Schumann, U., 1975: Subgrid scale model for finite difference simulations of turbulent flows in plane channels and annuli. *Journal of Computational Physics*, **18 (4)**, 376–404, https://doi.org/https://doi.org/10.1016/0021-9991(75)90093-5.

Sharma, A., and Coauthors, 2024: ExaWind: Open-source CFD for hybrid-RANS/LES geometry-resolved wind turbine simulations in atmospheric flows. *Wind Energy*, https://doi.org/10.1002/we.2886, to appear.

Smagorinsky, J., 1963: General circulation experiments with the primitive equations. *Monthly Weather Review*, **91 (3)**, 99–164, URL https://doi.org/10.1175/1520-0493(1963)091⟨0099:GCEWTP⟩2.3.CO;2.

Sprague, M. A., S. Ananthan, G. Vijayakumar, and M. Robinson, 2020: ExaWind: A multifidelity modeling and simulation environment for wind energy. *Journal of Physics: Conference Series*, **1452**, https://doi.org/10.1088/1742-6596/1452/1/012071, URL https://iopscience.iop.org/article/10.1088/1742-6596/1452/1/012071/pdf.

Stolz, S., P. Schlatter, and L. Kleiser, 2005: High-pass filtered eddy-viscosity models for large-eddy simulations of transitional and turbulent flow. *Physics of Fluids*, **17 (6)**, 065 103, https://doi.org/10.1063/1.1923048, URL https://doi.org/10.1063/1.1923048.

Sullivan, P., J. Edson, T. Hristov, and J. McWilliams, 2008: Large-eddy simulations and observations of atmospheric marine boundary layers above nonequilibrium surface waves. *Journal of the Atmospheric Sciences*, **65 (4)**, 1225–1245.

Sullivan, P., J. McWilliams, and C. Moeng, 1994: A subgrid-scale model for large-eddy simulation of planetary boundary-layer flows. *Bound.-Layer Meteor.*, **71**, 247–276.

Sullivan, P., J. Weil, E. Patton, H. Jonker, and D. Mironov, 2016: Turbulent winds and temperature fronts in large-eddy simulations of the stable atmospheric boundary layer. *Journal of the Atmospheric Sciences*, **73 (4)**, 1815–1840, https://doi.org/10.1175/JAS-D-15-0339.1.

Svensson, G., and A. Holtslag, 2009: Analysis of model results for the turning of the wind and related momentum fluxes in the stable boundary layer. *Boundary-Layer Meteorol*, **132**, 261–277, https://doi.org/https://doi.org/10.1007/s10546-009-9395-1.